1 **The CU 2D-MAX-DOAS instrument - part 2: Raman Scattering Probability Measurements and**

2 **Retrieval of Aerosol Optical Properties**

3

4 Ivan Ortega[1,2], Sean Coburn[1,2], Larry K. Berg[3], Kathy Lantz[2,4], Joseph Michalsky[2,4], Rich Ferrare[5],

5 Johnathan Hair[5], Chris Hostetler[5], and Rainer Volkamer[1,2]

6

7 [1]Department of Chemistry and Biochemistry, University of Colorado, Boulder, CO, USA

8 [2]Cooperative Institute for Research in Environmental Sciences (CIRES), Boulder, CO, USA

9 [3]Pacific Northwest National Laboratory, Richland, WA, USA

10 [4]Global Monitoring Division, Earth System Research Laboratory, NOAA, Boulder, CO, USA

11 [5]NASA Langley Research Center, Hampton, VA, USA

12

13 *Correspondence to:* Rainer Volkamer (rainer.volkamer@colorado.edu)

14

15 **Abstract**

16 The multiannual global mean of aerosol optical depth at 550 nm (AOD_{550}) over land is ~0.19, and that

17 over oceans is ~0.13. About 45% of the Earth surface shows AOD_{550} smaller than 0.1. There is a need

18 for measurement techniques that are optimized to measure aerosol optical properties under low AOD

19 conditions. We present an inherently calibrated retrieval (i.e., no need for radiance calibration) to

20 simultaneously measure AOD and the aerosol phase function parameter, *g*, based on measurements of

21 azimuth distributions of the Raman Scattering Probability (RSP), the near-absolute Rotational Raman

22 Scattering (RRS) intensity. We employ Radiative Transfer Model simulations to show that solar

23 azimuth RSP measurements are insensitive to the vertical distribution of aerosols, and maximally

24 sensitive to changes in AOD and *g* under near molecular scattering conditions. The University of

25 Colorado two dimensional Multi-AXis Differential Optical Absorption Spectroscopy (CU 2D-MAX-

26 DOAS) instrument was deployed as part of the Two Column Aerosol Project (TCAP) at Cape Cod,

27 MA, during the summer of 2012 to measure direct sun spectra, and RSP from scattered light spectra at

28 solar relative azimuth angles (SRAA) between 5° and 170°. During two case study days with (1) high

29 aerosol load (17 July, $0.3 < AOD_{430} < 0.6$) and (2) near-molecular scattering conditions (22 July,

30 $AOD_{430} < 0.13$) we compare RSP based retrievals of AOD_{430} and *g* with data from a co-located CIMEL

31 sun photometer, Multi-Filter Rotating Shadowband Radiometer (MFRSR), and airborne High Spectral

32 Resolution Lidar (HSRL-2). The average difference (relative to DOAS) for AOD_{430} is: $+0.012 \pm 0.023$

Atmospheric
Measurement
Techniques
Open Access
Discussions
EGU

33 (CIMEL), -0.012 ± 0.024 (MFRSR), -0.011 ± 0.014 (HSRL-2), and +0.023 ± 0.013 (CIMEL$_{AOD}$ −

34 MFSRS$_{AOD}$); and yields the following expressions for correlations between different instruments:

35 DOAS$_{AOD}$ = -(0.019 ± 0.006) + (1.03 ± 0.02)·CIMEL$_{AOD}$ (R^2 = 0.98), DOAS$_{AOD}$ = -(0.006 ± 0.005) +

36 (1.08 ± 0.02)·MFRSR$_{AOD}$ (R^2 = 0.98), and CIMEL$_{AOD}$ = (0.013 ± 0.004) + (1.05 ± 0.01)·MFRSR$_{AOD}$

37 (R^2 = 0.99). The average g measured by DOAS on both days was 0.66 ± 0.03, with a difference of

38 0.014 ± 0.05 compared to CIMEL. Active steps to minimize RSP in the reference spectrum help to

39 reduce the uncertainty in RSP retrievals of AOD and g. As AOD decreases, and solar zenith angle

40 (SZA) increases the RSP signal-to-noise ratio increases. At AOD$_{430}$ ~ 0.4 and 0.10 the absolute AOD

41 errors are ~0.014 and 0.003 at 70$^°$ SZA, and 0.02 and 0.004 at 35˚ SZA. Inherently calibrated, precise

42 AOD and g measurements are useful to better characterize the aerosol direct effect in urban polluted

43 and remote pristine environments.

44

1. Introduction

46 Atmospheric aerosol particles play a key role in the energy balance of Earth's atmosphere (IPCC,

47 2013). The aerosol optical depth (AOD), defined as a vertical integral of the aerosol extinction

48 coefficient from the earth surface to the top of the atmosphere, is an important input to assessments of

49 how the atmospheric aerosol burden affects the budget of incoming solar radiation in global climate

50 models (Hansen et al., 2002; Chung et al., 2005; McComiskey et al., 2008). McComiskey et al. (2008)

51 studied the sensitivity of aerosol direct radiative forcing using representative uncertainties in currently

52 established methods to measure aerosol optical properties. For a typical AOD uncertainty of 0.01 (best

53 case scenario expected for newly calibrated ground based radiometric instrument in the visible spectra

54 range; Eck et al., 1999; Holben et al., 1998), the error in the aerosol direct forcing is about 0.6 W·m^{-2}

55 (top of the atmosphere) and 1.3 W·m^{-2} (surface) for a solar zenith angle (SZA) of 45˚ (McComiskey et

56 al., 2008). The multiannual global mean AOD$_{550}$ estimated from satellites find that about 28% and 43%

57 of the land surface, and 15% and 46% of the ocean surface have AOD ≤ 0.05, and ≤ 0.1 (Remer et al.,

58 2008); current ground based networks capture frequent AOD values below 0.15 (Holben et al., 2001;

59 Augustine et al., 2008; Michalsky et al., 2010; Mao et al., 2014). Low AOD conditions are projected to

60 be more prevalent in the future (Westervelt et al., 2015). Under these conditions measurements of AOD

61 with higher accuracy and precision are even more desirable.

62 Traditional AOD measurements often employ radiometric calibrated instruments, e.g., CIMEL sun

63 photometer (Holben et al., 1998) and multifilter rotating shadowband radiometer (MFRSR) (Harrison et

Atmospheric
Measurement
Techniques
Discussions

Open Access

EGU

64 al., 1994). In general, the retrieval of AOD is estimated based on the extinction of the direct sun

65 irradiance measurements. The quality of such measurements is improved under high AOD and cloud

66 free conditions. On the other hand, under molecular scattering conditions, i.e., $AOD_{430} < 0.13$ (=

67 Rayleigh scattering extinction under overhead sun conditions), the measurements become subject to

68 higher relative uncertainties (Holben et al., 1998). Holben et al. (1998) pointed out that the error in

69 AOD by means of solar sky brightness (scattering) in the solar aureole region may be lower than

70 traditional direct sun extinction methods. However, to our knowledge, this has not previously been

71 exploited in measurements to date.

72 Multi-AXis Differential Optical Absorption Spectroscopy (MAX-DOAS) can simultaneously retrieve

73 trace gases and aerosol optical properties (Hönninger et al., 2004; Wagner et al., 2004; Frieß et al.,

74 2006; Clémer et al., 2010). The MAX-DOAS technique relies on spectrally resolved solar scattered

75 light measurements at several elevation angles (EA), defined between the horizon and zenith

76 (Hönninger et al., 2004). The retrieval approach does not require radiometric calibration, and the trace

77 gases and aerosol optical properties are measured relative to a reference spectrum, typically recorded in

78 the zenith. Measurements at low EA have maximum sensitivity in the lowermost part of the

79 atmosphere. More recently, two dimensional (2D) MAX-DOAS has been shown to be a promising

80 technique to measure the trace gas variability around the measurement site from scattered light spectra

81 at different Azimuth Angles (AA), defined relative to North (Wang et al., 2014; Ortega et al., 2015a).

82 The University of Colorado (CU-) 2D-MAX-DOAS instrument has demonstrated range resolved

83 measurements of NO_2 and oxygenated hydrocarbons from azimuth scans at low EA. The spatial scale

84 probed by 2D-MAX-DOAS closely resembles the grid-cell size of atmospheric models and satellite

85 pixels, and can be used to systematically characterize chemical gradients under inhomogeneous

86 conditions (Ortega et al., 2015a).

87 In this paper we exploit solar azimuth scattered light and direct-sun measurements to assess aerosol

88 column properties using solar almucantar measurements. The information content regarding aerosol

89 properties using this geometry has been discussed in detail for radiance measurements with single

90 wavelength channel detectors elsewhere (Box and Deepak, 1979; Nakajima et al., 1983; Kaufman et al.,

91 1994; Bohren and Huffman, 1998; Dubovik et al., 2000). We use solar almucantar scans in combination

92 with hyperspectral measurements, and describe a new retrieval scheme to estimate AOD_{430} and aerosol

93 phase functions (simplified by g, Henyey-Greenstein approximation) based on quantitative analysis of

94 the Rotational Raman Scattering (RRS) by atmospheric molecules (Ring effect) (Grainger and Ring,

Atmospheric
Measurement
Techniques
Discussions
EGU

95   1962; Chance and Spurr, 1997). RRS causes "filling-in" of the solar Fraunhofer lines, and has to be

96   taken into account to accurately estimate absorption of trace gases using passive DOAS techniques

97   (Platt and Stutz, 2008). The quantitative analysis of RRS by DOAS was introduced by Wagner et al.

98   (2004, 2009a) with the so-called "Raman Scattering Probability" (RSP) (the probability that a detected

99   photon has undergone a rotational Raman scattering event). Under cloud free conditions the AOD has a

100   strong effect on the RSP, which further exhibits a high dependency on the solar relative azimuth angle

101   (Wagner et al., 2009b; Wagner et al., 2014). To the best of our knowledge, there has been no previous

102   measurement of AOD and g using almucantar scans of RSP by MAX-DOAS.

103   **2. Experimental**

104   **2.1   The TCAP field campaign**

105   The first phase of the Department of Energy (DOE) Two-Column Aerosol Project (TCAP) field

106   campaign took place at Cape Cod, MA during the summer of 2012 (Berg et al., 2015). TCAP was

107   designed to provide a comprehensive characterization of the aerosol direct and indirect effects under

108   urban emission influences near the east coast of North America (over Cape Cod, MA), and to contrast it

109   with observations in pristine conditions over the Atlantic Ocean. An extensive set of aerosol

110   measurements were conducted aboard two research aircrafts (DOE G-1 and NASA B200) and with the

111   DOE Atmospheric Radiation Measurement (ARM) ground Mobile Facility (located over Cape Cod,

112   MA, U.S.); for details see Berg et al. (2015). The CU 2D-MAX-DOAS was deployed at the ARM

113   ground site from 1 July to 13 August 2012 to test its innovative capabilities to measure aerosol optical

114   properties and trace gases simultaneously with a single instrument. Here, we focus primarily on 22 July

115   2012 due to its low AOD and cloud free conditions, and the available complementary data (Berg et al.,

116   2015; Ortega et al., 2015b). The retrieval approach is also applied for a high AOD case study on 17

117   July 2012. The TCAP data set provides an excellent opportunity to evaluate the robustness of the RSP-

118   based retrieval approach and to compare the products with independent instruments. Table 1 and

119   Section 2.6 present other measurements and products used in this work.

120

121   **2.2   2D-MAX-DOAS measurements**

122   The 2D-MAX-DOAS telescope and detection system has been described in detail elsewhere (Ortega et

123   al., 2015a). The angles defining the geometry of measurements are illustrated in Fig. 1. The CU 2D -

124   MAX-DOAS instrument conducts measurements in three different modes: (1) off-axis scan where

125   several elevation angles (EA) and zenith are used with a fixed azimuth angle (AA) relative to north; (2)

Atmospheric
Measurement
Techniques
Discussions

126   almucantar scan, where solar scattered photons are collected using any EA for multiple solar relative

127   azimuth angles (SRAA). To further enhance the aerosol information content and estimate uniformity

128   (homogeneity) around the measurement site the almucantar scan is carried out on the left and right side

129   of the solar disc. Up to now, this particular geometry has not been used with MAX-DOAS, however it

130   is widely used by the CIMEL sun photometer using single wavelength channel detectors at solar

131   elevation (EA = 90° - SZA) (Holben et al., 1998); and (3) direct sun observations, which inherently

132   minimize RSP.

133   The 2D-MAX-DOAS instrument deployed during TCAP at the ARM Mobile Facility consisted of three

134   synchronized spectrograph/detector units located indoors in a temperature controlled sea container, the

135   control measurement laptop, and the 2D telescope located outdoors. The telescope was deployed on top

136   of one seatainer (~45 m ASL) providing an unobstructed view close to the horizon in a ~360° azimuth

137   view. The only small obstruction in the azimuth scan was an independent sampling inlet pillar located

138   in the middle of the seatainer. The light collected with the telescope was focused onto a single

139   CeramOptics 25 m x 1.0 mm silica mono fiber coupled to a tri-furcated fiber bundle connected to three

140   Ocean Optics (QE65000) spectrometers collecting solar light between 300 and 631 nm with a spectral

141   resolution between 0.4 - 0.6 nm (FWHM). The same spectrometer system was used in the remote

142   Pacific Tropical Ocean for the detection of glyoxal (Sinreich et al., 2010). The electronic rack

143   containing the spectrograph/detectors was temperature controlled (34 °C, 0.005 °C peak to peak

144   variation) and CCDs cooled to -30 °C to minimize dark current.

145   **2.2.1   Configuration of the azimuth scan**

146   The instrument was configured to conduct measurements of direct sunlight, and scattered sunlight using

147   a sequence of EA and AA pairs described in Table 2. The off-axis scan consisted of 7 EAs and zenith,

148   and spectra were recorded using an integration time of 1 min at each angle alternating South and North

149   AAs (total acquisition time of 16 − 17 min). This specific geometry was used in order to know the

150   effect of elevated aerosol layers in the apparent absorption of the oxygen collision complex (O_2-O_2) as

151   seen by the 2D-MAX-DOAS (Ortega et al., 2015b). At the end of the EA scan, the almucantar scan was

152   implemented with an integration time of 1 s with 70 angles relative to the sun in steps of 5° up to 180°

153   on the left and right sides of the solar disk at solar EA. The almucantar scan was repeated for a fixed

154   EA of 45°. The total acquisition time of the azimuth scan was 2 - 3 min. In this work, we focus only on

155   the almucantar scan at solar EA. The full measurement cycle between EA and almucantar scans took

156   about 20 min and was repeated sequentially. The initial solar almucantar alignment procedure to

157   achieve pointing accuracy better than the motors internal encoder resolution (0.17°) is described in

158   detail by Ortega et al. (2015a). Briefly, the initial alignment is carried out in the field by measuring

159   rapid (1 s, integration time) solar scattered spectra with several small SRAA (usually -5° < SRAA < 5°,

160   negative SRAAs are left and positive values are right side of the sun). The alignment is achieved when

161   measurements of intensities (in counts·s^{-1}) on the right and left sides present symmetry and the offset

162   estimated with a Gaussian fit of the intensities at the center of the sun's disk is small (< 0.17°) and

163   accounted in the software. To avoid saturation of the detector, this alignment procedure was performed

164   below and above the sun position (see Fig. 2 in Ortega et al., 2015a). The telescope field of view (FOV)

165   of this viewing port was determined by introducing light into the fiber retrospectively from the exit

166   side, and the divergence of the light after exiting the telescope was evaluated to have a full opening

167   angle of 0.6° in agreement with the theoretical FOV based on the experimental field setup.

168   **2.2.2   Direct sun mode**

169   During the first phase of TCAP, for cloud-free days, direct sun spectra were recorded periodically with

170   a total integration time of 2 - 4 min. In order to reduce the intensity of the direct sun beam and avoid

171   saturation of the detector the light is collected via an integrating sphere with a diameter of 2.54 cm. The

172   sphere also serves for correcting pointing inaccuracies and atmospheric lens effects (Herman et al.,

173   2009). To minimize the contribution of solar scattered photons in the direct sun mode a black anodized

174   collimator tube with a full opening angle of 2.9° was used. A sketch of the optics housed integrating the

175   direct sun and azimuth ports is shown in Fig.1 in Ortega et al. (2015a). The custom software developed

176   in LabView uses the exact coordinate location and heading (defined as zero corresponding to true

177   north) to operate the 2D telescope. This information is used as Euler angles to correct the astronomical

178   solar position and locate the sun in the sky. This step is similar to the crude alignment of advanced solar

179   trackers, which apply active imaging of the solar disk for precise pointing (Gisi et al., 2011; Baidar et

180   al; 2015). We do not aim to track the sun in this work. The purpose of the direct sun mode is to obtain

181   spectra that are near-free of RRS, and use these direct sun spectra as reference spectra in the retrieval of

182   RSP. To assess pointing accuracy of the direct sun observation we use the solar azimuth scan alignment

183   as explained in section 2.2.1.

184

185   **2.3   DOAS retrieval of differential RSP and intensities**

186   The main products retrieved with the solar azimuth scan are the non-calibrated spectral intensities

Atmospheric
Measurement
Techniques
Discussions

187   (I_{norm}) and the strength of RRS by atmospheric molecules (RSP). The spectra intensities were corrected

188   by electronic offset and dark current, and the number of CCD-pixel counts were normalized by the

189   integration time (units of counts$\cdot$s^{-1}) at a certain wavelength (λ). These normalized I_{norm} are used for

190   quality assurance of homogeneity and to calculate pointing accuracy only. The differential RSP (dRSP;

191   differential with regards to the amount contained in the reference spectrum) was measured by its

192   specific narrow band signatures (< 1 nm) at UV-Vis wavelengths (Fig. 2), which are separated well

193   from broadband molecule and aerosol extinction using the DOAS method (Platt and Stutz, 2008). We

194   follow the retrieval strategy introduced in Wagner et al. (2009a) and apply the DOAS settings from

195   Wagner et al. (2009b) to retrieve the RSP in the fitting window of 426 – 440 nm. The only atmospheric

196   cross section absorber adjusted to the spectrometer resolution that is included in the analysis is NO_2

197   (Bogumil et al., 2003). A third order polynomial is fitted to account for broad band spectral structures.

198   A direct sun spectrum recorded at low SZA (28˚) on 22 July 2012 is used as reference spectrum to

199   evaluate the dRSP in the azimuth scan mode. The Ring cross section is calculated from the respective

200   sun-observation spectrum using the DOASIS software (Kraus, 2006), which then is normalized by

201   removing the continuum component with a third order polynomial high pass filter (Wagner et al.,

202   2009a). The spectra were analyzed using the WinDOAS software package (Fayt and Van Roozendael,

203   2001).

204   An example of the DOAS fit analysis is shown in Fig 2. Systematic errors in the retrieval of dRSP were

205   quantified by means of sensitivity studies. The sensitivity of the DOAS settings were explored by

206   changing the wavelength intervals and polynomial orders in a similar way as performed by Vogel et al.

207   (2013). These sensitivity tests reveal a remarkable stability towards changing the DOAS fitting window

208   using different polynomial orders (see Fig. S1; difference < 5%; the same analysis in the UV, Fig. S2,

209   yields two times greater DOAS fit error and root mean square (RMS) due to the smaller signal to noise

210   ratio achieved with 1 s integration time). The typical value of the dRSP fit error is ~0.0018, calculated

211   internally in WinDOAS as the standard deviations on the retrieved dRSP; it interestingly does not

212   depend strongly on the SRAA. We adopted this uncertainty in the final error propagation of the aerosol

213   optical properties (see section 3.3.1).

214   Figure 3 shows typical examples of the measurements of dRSP and I_{norm} obtained with the solar

215   azimuth scan (mode 2) for three different SZAs. The SRAA scan is from -180˚ (left side of the sun) to

216   +180˚ (right side of the sun). The dRSP decreases for small SRAAs due to fewer scattering events by

217   molecules and a dominant aerosol forward scattering. On the other hand the I_{norm} increases for small

Atmospheric
Measurement
Techniques
Discussions

Open Access

EGU

218   SRAAs due to the strong probability of aerosol scattering in the forward direction. The second

219   important aspect is the SZA dependency. Previous studies have established the relationship between the

220   SRAA, SZA and the effective aerosol scattering angles (Nakajima et al., 1996; Torres et al., 2013). In

221   general, the information content of the azimuth scan is maximized by using high SZAs. The maximum

222   dRSP values (corresponding to a minimum I_{norm}) are shown at SRAA of 100˚ (for SZA = 66˚), which

223   indicates to some degree the high sensitivity to aerosol scattering processes (aerosol phase function).

224   The dRSP decreases for low SZA (blue circles).

225   **2.4   Radiative Transfer Simulations**

226   We use the full spherical Monte-Carlo atmospheric radiative transfer model (McArtim) (Deutschmann

227   et al., 2011) to simulate and interpret the measurements. McArtim has been successfully tested and

228   compared with other radiative transfer models (Wagner et al., 2007). McArtim simulates atmospheric

229   photon transfer using the optical properties described by several input parameters such as vertical

230   profiles of pressure, temperature, and aerosol extinction characterized with aerosol phase functions,

231   typically represented by g, and single scattering albedo (SSA). McArtim calculates the absolute RSP

232   using the fraction of scattering events that have presented RRS (inelastic scattering). Reflection at the

233   surface is characterized with the surface albedo (SA) and is treated as Lambertian. The modeled RSP

234   from McArtim has been previously characterized and used in several studies (Wagner et al., 2009b;

235   Wagner et al., 2010; Wagner et al., 2014). Several general input parameters are required and kept

236   constant in the forward modeling. An altitude grid of 100 m up to 10 km, 200 m up to 50 km, and 5 km

237   up to 100 km was used. The FOV was set to 0.6˚ (similar to the full opening angle of the telescope, see

238   section 2.2.1). The wavelength chosen to forward model the RSP is 430 nm representing the middle

239   wavelength of the fitting window and characteristic Ca-lines of the Fraunhofer spectrum (Wagner et al.,

240   2010). In this section we describe the different sensitivity studies that were performed in order to

241   understand the effect of aerosol optical properties in the measured RSP using the solar azimuth scan

242   geometry. For the sensitivity studies we use the pressure, temperature, and RH profiles taken from the

243   U.S Standard Atmosphere. We have adopted the geometry of typical 2D-MAX-DOAS measurement

244   taken from TCAP, i.e., similar SRAA angles (-180 to +180˚) and SZA ranges.

245

246   **2.4.1   Sensitivity of RSP to aerosol distribution**

247   Figure 4A presents the effect of AOD on the simulation of RSP in the azimuth scan for a single SZA

248   (70˚). Additional input properties are SSA = 0.98, g = 0.70, SA = 0.05, and homogeneous extinction

Atmospheric
Measurement
Techniques

Open Access

EGU

Discussions

249   height of 1.5 km. As expected (see Fig. 3), the RSP decreases and the radiance increases for angles

250   close to the sun (see Fig. 4A). In general, the RSP decreases with increasing AOD due to the decrease

251   of molecular scattering and higher probability of aerosol elastic scattering (see section 3.3 for further

252   analysis regarding maximal low AOD information). Figure 4A also shows that the maximum RSP is at

253   about $90 - 100°$, in agreement with our measurements at similar SZA (see Fig. 3A). Figure 4B shows

254   the sensitivity of the RSP with respect to the aerosol extinction vertical distribution while keeping the

255   AOD constant at 0.2 (additional parameters are the same as before). Several homogeneous extinction

256   vertical profiles from altitudes of 0.5 to 2.0 km are studied as well as a case of aerosol extinction aloft,

257   assuming maximum extinction at 2.8 km with a width of 2.8 km. Similar results are obtained also at

258   small SZA (see Fig. S3). It is clear that the aerosol extinction vertical distribution does not play a

259   significant role in the simulation of RSP in the azimuth scan. Systematic elevated aerosol extinction

260   layers were identified during TCAP (Berg et al., 2015; Ortega et al., 2015b). Previous studies have

261   shown that RSP is primarily sensitive to the AOD (Wagner et al., 2009b), and recognize the value of

262   measurements at small SRAA to obtain information about g (Holben et al., 1998; Wagner et al., 2009b).

263   The sensitivity studies in Figs 3, 4, and in the supplement confirm that the RSP does not depend on the

264   aerosol vertical distribution. Hence, the RSP is suitable to characterize column properties of AOD and

265   the aerosol phase function, g. The elevated aerosol layers documented by Berg et al. (2015) during

266   TCAP hence are captured, and do not present a limitation for this work.

267   **2.4.2   Sensitivity to g, SSA, and SA**

268   The second sensitivity study aimed to understand the effect of g, SSA, and SA. Figure 5 shows the

269   results of the RSP and Sun-normalized radiances, R_{norm} (sr^{-1}), defined internally in McArtim as the ratio

270   of the radiance ($W·m^{-2}·sr^{-1}$) of the geometry indicated to the solar irradiance ($W·m^{2}$) using a

271   homogeneous aerosol extinction profile with an AOD of 0.2 (box height of 1.5 km), and SZA of 70°.

272   The asymmetry parameter, g, has the strongest effect on the RSP, especially for SRAA < 40°. The

273   importance to the RSP of the geometry of measurements and its qualitative sensitivity towards aerosol

274   phase functions was identified by Wagner et al. (2009b) using three different fixed azimuth directions.

275   The RSP does not show a significant variability among different SSA, i.e., aerosol composition,

276   however the sun-normalized radiances show some sensitivity among all SRAA, especially with angles

277   close to the sun where variability of up to 10% are found. A similar sensitivity study was shown in

278   Frieß et al. (2006). The SA does not play a significant role in the simulation of either the RSP or

279   radiances. Further discussion of the phase functions is presented in section 3.3.2.

280 **2.5   Retrieval of AOD and *g***

281 As shown before, maximal sensitivity towards AOD and aerosol phase function is achieved using the

282 solar azimuth scan. The aim of this study is to develop a simple strategy in order to retrieve AOD and

283 aerosol phase function, *g* while constraining SSA and SA. A simple method would be to compare the

284 measurements with the RTM simulations and optimize the aerosol input parameters until we minimize

285 the differences between measurements and simulations. An iterative approach for a single SRAA scan

286 would require several hours to finalize. For a typical single day of measurements during the TCAP we

287 collected at least 3500 spectra using only the azimuth scan. In this context, we believe that a flexible

288 option is the creation of a look up table (LUT) where the RSP is simulated using geometry related

289 inputs and numerous aerosol optical properties.

290

291 We created the LUT based on different sets of SZA (20° to 90° in steps of 10°) and adopted the positive

292 SRAA as measured by the 2D-MAX-DOAS. The parameters that were fixed are the SSA, 0.98, based

293 on findings by Müller et al. (2014) and Kassianov et al. (2014) during TCAP. The SA was set to 0.05

294 representative of the land surface (obtained from the atmospheric transmission by the co-located

295 MFRSR), and the aerosol extinction height (homogeneous box-height of 1.5 km), though any other

296 height would give similar results. We use a typical pressure, temperature, and RH profiles (up to an

297 altitude of 28 km) measured from radiosondes during TCAP (Berg et al., 2015). Above 28 km the U.S

298 standard atmosphere was used. The range of parameters that are important and were changed are the

299 AOD_{430} and *g*. The range of AOD covered was from 0 up to 2.0 AOD in steps of 0.02. The range of *g*

300 covered was from 0.64 to 0.72 with increments of 0.02. In order to compare with the measurements the

301 LUT is interpolated to fine grid set points of AOD (in steps of 0.005) and to the average SZA during

302 the measurements. The AOD and *g* are varied to minimize the following expression:

303

$$\chi^2 = \sum_{i=1}^{N} \frac{[RSP_M - RSP_{LUT}(AOD, g)]_i^2}{RSP_e^2} \rightarrow min \qquad (1)$$

304

305 where RSP_M and RSP_{LUT} are the RSP (arb. units) measured and the simulated in the LUT. RSP_e is the

306 final estimated RSP error in the measurements (see sect 3.3.1) and *N* represents the number of SRAAs.

307 A detailed representation of the sensitivity of RSP towards AOD using the SRAA scan and several SZA

308 is shown in the supplemental information (see Fig. S4).

309

Atmospheric
Measurement
Techniques
Discussions

Open Access

EGU

2.6 Additional measurements

310

311　The co-located MFRSR (Harrison et al., 1994) and the CIMEL sun photometer (Holben et al., 1998)

312　complement our AOD observations at the TCAP ground site (see details in Table 1). The MFRSR

313　measures total and diffuse solar irradiances at several channels to infer the direct solar radiation

314　component (time resolution of 1 min) while the Sun Sky photometer instrument measures the direct

315　solar beam (time resolution of about 5 min). While both instruments are radiometrically calibrated and

316　work under different principles, a common feature is that they both use the direct sun transmission to

317　derive AODs (Holben et al., 1998; Harrison et al., 1994). The AOD_{430} was calculated using the

318　extinction Angstrom exponent between the standard spectral bands of each instrument (see Table 1).

319　The second generation airborne High Spectral Resolution Lidar (HSRL-2), an improved version of the

320　HSRL-1 (Hair et al., 2008), was deployed aboard the NASA Langley Research Center B200 King Air

321　airplane. HSRL-2 measures particle backscatter coefficients at 355, 532, and 1064 nm, and particle

322　extinction coefficients at 355 and 532 nm (Müller et al., 2014). Similar as the sun photometer, the AOD

323　at 430 nm was calculated using the extinction Angstrom exponent between the standard wavelengths of

324　355 and 532 nm. Atmospheric temperature and pressure profiles were provided by local radiosondes,

325　which were launched four times a day at the ground site (~ 00, 05, 17, and 23 UTC). The measurement

326　vertical resolution of the sondes was about 10 m reaching a maximum altitude of about 28 km. For this

327　study, the closest radiosonde in time (17 UTC or 13:00 local standard time, LST = UTC-4) is used to

328　prescribe the temperature, pressure and relative humidity in the RTM.

329

3. Results and discussions

330

331

3.1 Effect of the reference spectrum

332

333　The direct sun geometry contains a small amount of RRS light, and is hence not free of RSP

334　contribution. In order to assess the RSP contribution in the direct sun spectra we use two different

335　approaches: (1) a Langley plot type method, where the dRSP obtained with direct sun spectra as

336　reference spectrum is plotted as a function of the SZA, and (2) by interpolating the dRSP measured

337　with small SRAA to the 0° (direct sun view). Fig. 6 shows the linear correlation analysis between the

338　direct sun dRSP (binned by SZA) measured on 22 July 2012, low AOD_{430} case (< 0.13), and the air

339　mass factor (AMF), $AMF = 1/\cos(SZA)$. Several direct sun measurements were carried out between

340　SZA of 22° (AMF =1.06) and 47° (AMF < 1.47) and only one at 78° (AMF = 4.8). In order to

Atmospheric
Measurement
Techniques
Discussions

341   quantitatively estimate the RSP in the reference we use the linear correlation analysis applied for SZA

342   smaller than 50˚ ($R^2 = 0.98$) (see inset plot in Fig. 6). The extrapolation to AMF = 0 yields the absolute

343   value of the RSP contained in the reference spectrum (RSP value if there were no atmosphere), which is

344   determined as 0.0053 ± 0.0007 by this method. The value of dRSP at high SZA (78˚) is not considered

345   here, since there is only one data point and the magnitude is significantly larger (likely due to

346   atmospheric changes and increasingly distant air masses). To estimate the RSP contained in the

347   reference with the second method we have analyzed closely the RSP measurements using the solar

348   azimuth scan for SZA < 45˚ and SRAA close to the sun (SRAA < 40˚). The RSP decreases linearly for

349   angles close to the sun and an interpolation to 0˚ SRAA yields an RSP value of 0.0035 ± 0.0005. We

350   use the average of the two methods (0.0044 ± 0.0012) and add this offset to the measured dRSP to

351   calculate the absolute RSP for comparison with RTM. For assessment of the RSP error, we propagate

352   the 2-sigma standard deviation (0.0024) in the final uncertainty of RSP_e and in error of AOD and g

353   products (see section 3.3.1).

3.1.1 Comparing direct-sun and zenith reference spectrum

355   To assess the effect of the reference spectrum in the DOAS analysis of the dRSP we compare the dRSP

356   results using the zenith and direct sun spectra as references; both spectra were recorded at SZA of 28˚.

357   Figure S5 shows the linear correlation of the dRSP analysis using each reference to analyze all spectra

358   recorded for azimuth scans for SZA smaller than 70˚ on 22 July 2012. We find a strong linear

359   correlation ($R^2 \geq 0.99$) and a slope close to unity (1.023 ± 0.001). The negative offset corresponds to

360   1.9 % RSP contained in the zenith reference relative to the direct sun. Wagner et al. (2009b) estimated

361   an RSP of 5 ± 1% in the UV (350 nm) in the noon zenith sky reference by means of RTM simulations

362   using an AOD of 0.1 measured by a co-located instrument. The strength of the RSP depends on several

363   factors such as wavelength, the atmospheric conditions (aerosol and cloud optical properties), and the

364   geometry of measurements. The dRSP in Fig. S5 is color coded by SRAA. The strong SRAA

365   dependency reflects the sensitivity of RSP to atmospheric scattering processes. The dRSP decreases for

366   angles close to the sun and increases for larger SRAA. When using the zenith sky as reference the dRSP

367   obtained would be negative for SRAA < 50˚ and there would be a general negative bias of 1.9 %. Of all

368   possible viewing directions accessible with ground based measurements the direct sun observation is

369   the least affected by RRS. In addition, direct sun observations measured with the same instrument

370   ensure that the spectral resolution and sampling used in the DOAS analysis of all spectra are the same.

3.1.2 Calculating references from high-resolution spectra

Atmospheric
Measurement
Techniques
Open Access
Discussions
EGU

372   In principle, high resolution solar spectra (e.g., Chance and Kurucz, 2011) should provide a viable

373   alternative to direct-sun measurements as reference spectra to retrieve absolute RSP. Such high

374   resolution spectra need to be convoluted with the instrument slit function prior to their use as reference

375   spectrum in the DOAS analysis of RSP. We have tested this approach and used high resolution

376   literature data as a reference spectrum for the analysis of the azimuth scan spectra (1 s integration time),

377   and find large fitting residuals (RMS ~0.01), that have a strong effect on the retrieved RSP values,

378   suggesting that this approach is currently of limited value in practice. The causes are likely due to a

379   combination of reasons, including imperfect knowledge about the wavelength dependent instrument

380   line shapes, numerical artifacts and assumptions made during convolution, non-linearity of detectors,

381   and small differences in wavelength calibration. Notably, measuring the direct-sun reference spectrum

382   in the same instrument as the scattered light spectra inherently accounts for these factors.

383   **3.2 Effect of aerosol inhomogeneity**

384   The RTM simulation of RSP and R_{norm} considers aerosol to be uniformly distributed around the

385   measurement site. To assess if the air mass probed is inhomogeneous we compare quantitatively the

386   symmetry of the I_{norm} measurements to the left and right side of the sun's disk. The quantitative analysis

387   of symmetry is defined by the angular asymmetry factor parameter ($AFP_{I_{norm}}$)

388

$$AFP_{I_{norm}} = \frac{(I_{norm}^L - I_{norm}^R)}{(I_{norm}^L + I_{norm}^R) \cdot 0.5} \qquad (2)$$

389

390   where I_{norm}^L and I_{norm}^R are the left and right side measurements of the I_{norm} (counts s^{-1}) obtained with

391   the almucantar scan. The $AFP_{I_{norm}}$ on 17 and 22 July 2012 are shown in the form of a polar plot in Fig.

392   S5. Over the past few years, CIMEL sun photometers have used a similar approach as a consistency

393   check to reject pairs of data that exceed 20 % difference and under uniformity the retrieval inversion of

394   aerosol microphysical properties is applied (Holben et al., 1998). Both days show $AFP_{I_{norm}}$ < 10 %,

395   indicating a high degree of symmetry. In general, the random noise in $AFP_{I_{norm}}$ is on the order of

396   0.25%. If the $AFP_{I_{norm}}$ shows consistent positive and/or negative values among several SRRAs this

397   may indicate aerosol inhomogeneity. For example, the increase in AOD at ~ 12:00 LST on 17 July was

398   accompanied by an average $AFP_{I_{norm}}$ of +2.7 % for the corresponding solar azimuth scan, and

399   maximum $AFP_{I_{norm}}$ of +10 % at 105˚ < SRAA < 145˚, indicating higher AOD in the south westerly

400   direction. Ortega et al. (2015b) examined the aerosol extinction inhomogeneity using HSRL-2 data

401   from overpasses above the TCAP ground site, and found that the AOD varied by about 10 % across the

402   site at ~13:00 LST on 17 July 2012. By contrast, on 22 July there were no significant differences

403   visible in the HSRL-2 data, and the symmetry remains all day with average $AFP_{I_{norm}}$ of 0.19 %, and a

404   standard deviation of 3.3 %.

405

406   **3.3 Uncertainty of RSP retrievals of AOD and g**

407   **3.3.1   RSP retrieval of AOD: maximal sensitivity at low AOD**

408   Figure 7 shows the simulated RSP in the solar azimuth scan as a function of AOD. The highest

409   response in RSP to changes in AOD is observed at low AOD, i.e., under conditions when Rayleigh

410   scattering extinction dominates over aerosol extinction. The sensitivity is highest for small SRAA. A

411   change of 0.01 AOD when molecular scattering dominates ($AOD_{430} < 0.1$) yields a considerable

412   decrease in the RSP ($\Delta RSP = 0.004$) for SRAA < 35°. This change is significantly greater than the

413   DOAS fit error of 0.0018 presented in section 2.3. The sensitivity decreases for SRAA > 35° but still

414   up to a SRAA of 70° the same change in AOD yields a significant (measurable) RSP response. On the

415   other hand, the sensitivity towards changes in AOD is weaker for AOD greater than 0.3, especially for

416   low SZA, and for small SRAAs. This is likely due to the dominance of aerosol scattering and few

417   molecular scattering events. While the reduced sensitivity can in principle be circumvented by

418   evaluating larger SRAA, such analysis puts more stringent criteria on aerosol homogeneity. The

419   absolute error in the AOD for any particular SRAA (AOD_e^i) was calculated as:

420

$$AOD_e^i = \left(\frac{RSP_e}{RSP^i}\right) \cdot AOD \qquad (3)$$

421

422   where RSP^i is the RSP in the ith SRAA and RSP_e is calculated as the error in the RSP propagated from

423   the DOAS measured RSP error (~0.0018) and the error in the estimation of the RSP in the reference

424   (0.0024). Assuming the errors of the measurement to be additive, the final RSP_e is about 0.0028.

425   Equation 3 is applied to all SRAAs and set of AODs from Fig. 7A. Figure 7B shows the calculated

426   absolute error in AOD (AOD_e) using all elements from Fig. 7A and weighted as follows:

427

$$AOD_e = \frac{\Sigma \left(\frac{AOD_e^i}{RSP_e}\right)^2}{\Sigma \left(\frac{1}{RSP_e}\right)^2} \qquad (4)$$

428

429   The weighted RSP relative error $\left(\frac{RSP_e}{RSP^i}\right)$ following the same approach is also shown in percentage in

430   Fig. 7B. Under high AOD conditions (~ 0.4) the absolute AOD_e is 0.02. The AOD_e decreases

431   significantly for AOD ≤ 0.1, with uncertainties of about 0.004 at AOD of 0.1, and 0.0025 at AOD of

432   0.05. As mentioned before the information content on aerosols using the solar azimuth scan is

433   enhanced at large SZA when RSP values are larger. At SZA = 70˚ (Fig. 7C), the errors decrease further

434   for low AOD as is illustrated in Figure 7D. The AOD_e is 0.014, 0.003, and 0.002 for an AOD of 0.4,

435   0.1, and 0.05, respectively. The error scales roughly with $\cos(SZA)$, indicating that the highest

436   sensitivity of RSP based AOD retrievals is at high SZA and low AOD.

437

438   **3.3.2   Aerosol phase function**

439   As shown in Figure 5, the phase function parameter g has the strongest effect on the simulated RSP for

440   small SRAA. A decrease of the g parameter, i.e., decrease of aerosol forward scattering probability,

441   leads to an increase of the RSP due to a higher contribution of molecular scattering at this direction.

442   The radiances also show a significant sensitivity towards g for small SRAA, as previously shown by

443   Frieß et al. (2006). For a fixed AOD and a change in g of ± 0.04 the RSP difference is about 0.03 for a

444   SRAA of 5˚, which is two times greater than the RSP error. In general, measurements at small SRAA

445   carry most information, and are highly recommended (Holben et al., 1998; Frieß et al., 2006). In

446   addition, the quality of the retrieval of g is expected to improve for high SZAs when there is an

447   increase in the information content of the scattering angle coverage (Torres et al., 2013; Dubovik et al.,

448   2000).

449

450   **3.4   Comparison of measurements and simulations**

451   We compare simulated and measured RSP for several SRAA ranges in Fig 8. The example shown in

452   Fig. 8 is obtained by applying the retrieval approach explained in section 2.5 for the solar azimuth scan

453   (SZA = 66.5˚) on 22 July 2012. Four sets of SRAAs are used: (A) 5˚ to 20˚, (B) 5˚ to 60˚, (C) 5˚ to

454   120˚, and (D) 5˚ to 170˚. Three values for g are used to show the sensitivity towards the phase function.

455   The AOD retrieved with each g is shown in the label box. The residuals, defined as the difference

456   between measured and simulated RSP (minimizing equation 1) are shown in the bottom panel below

457   each comparison. The gray shaded area (behind the residuals) represents the RSP error (± 0.0028)

458   defined before. The computed RMS errors (RMSE) are also shown. The comparison of the RSP

459   constrained by few SRAAs (< 20˚, Fig. 8A) show that all the residuals lie within the error bars

Atmospheric
Measurement
Techniques
Discussions

460   independently of g. However, the variability of the retrieved AOD is significant for each g and

461   maximum ΔAOD of 0.025 is obtained. When using more SRAAs (Figures 8B, 8C, 8D) the spread in

462   AOD values is reduced. The maximum ΔAOD obtained with using either 5˚ to 60˚, 5˚ to 120˚ or 5˚ to

463   170˚ SRAAs is 0.010. Significant residuals (greater than the RSP error) are obtained for g larger than

464   0.68. The residuals obtained with the g of 0.64 are always within the error bars of the measured RSP

465   indicating that this g (for SRAA < 40˚) is in excellent agreement with the g of 0.65 reported by the

466   CIMEL sun photometer close to this time. This further suggests that SRAA close to the sun are needed

467   and essential in order to maximize the sensitivity of the aerosol phase functions.

468

469   **3.5   Optimized observing strategy**

470   We have optimized a retrieval strategy such that at high SZA (> 50˚) we use SRAA in the range of 5˚ to

471   60˚, and for smaller SZA we use the full azimuth scan (5˚ < SRAA < 170˚). This was motivated by the

472   fact that for 5˚ < SRRA < 60˚ the AOD and g are stable, and show the minimal RMSE and maximal

473   information content at high SZA for this range. On the other hand less information content is achieved

474   at low SZA and more SRAA are needed. This optimization may be important in the presence of broken

475   clouds. In this case, as long as there is homogeneity for SRAA < 60˚ the retrieval strategy presented

476   here may yield good results.

477   TCAP represented the first deployment of the CU 2D-MAX-DOAS instrument. The geometry of

478   measurements was motivated by retrieving simultaneously trace gas and aerosol extinction profiles by

479   means of the EA scan and by testing the solar azimuth scan for the first time (table 2). The acquisition

480   time of the solar azimuth scan was 2 min. However the time resolution of the retrieved products is

481   about 20 min due to the 85 % duty cycle of the EA scan in the single repetition of both EA and solar

482   azimuth scan. The fast mode of measurements in the almucantar limits the retrieval of many typical

483   DOAS species such as the oxygen dimer (O_2-O_2, or O_4) and other trace gases (such as NO_2, HCHO,

484   CHOCHO, etc). Incrementing the time resolution in the solar azimuth scan would mean that O_4 could

485   be measured and have an additional piece of information in the retrieval of aerosol

486   optical/microphysical properties. Future deployments may consider a combination of SRAA scans

487   with longer integration time to also obtain trace gases, and EA scans for a subset of SRAA to obtain

488   trace gas vertical profiles. In addition, future deployments with 2D capabilities might consider the

489   solar principal plane sky geometry, which is similar to the almucantar scan but in the principal plane of

490   the sun (see Holben et al., 1998). This geometry would be very similar to the typical off-axis scan, i.e.,

491   high sensitivity towards the lower part of the atmosphere. In addition SRAA would be measured

492   giving information about phase functions. Furthermore, a future deployment may dedicate a full day to

493   direct sun observations in order to apply the Langley plot to more SZA, ideally during constant diurnal

494   AOD conditions such as in Mauna Loa, HI.

495

496   **3.6   Comparison with CIMEL sun photometer, MFRSR, and HSRL-2**

497   Figure 9 compares the diurnal variability of AOD_{430} and g with independent measurements by

498   MFRSR, CIMEL sun photometer, and HSRL-2 instruments for (A) 22 July (low AOD case) and (B) 17

499   July (high AOD case) 2012. The molecular scattering optical depth represented with the discontinuous

500   gray line is calculated with the method reported by Bodhaine et al. (1999) using the temperature and

501   pressure profiles from the local radiosonde (launched at 13:00 LST). Considering a diurnal direct sun

502   geometry the molecular scattering optical depth is weighted by the air mass factor $1/\cos(SZA)$. On 22

503   July the retrieved aerosol AOD_{430} is below the molecular scattering regime all of the day for MFRSR,

504   DOAS and HSRL-2, and most of the time for the CIMEL sun photometer. Under these conditions the

505   uncertainties of the AOD retrieved from the solar beam extinction approach, i.e., MFRSR and CIMEL

506   sun photometer, might be greater than 0.01 AOD, which is a typical error after calibration (Holben et

507   al., 1998; Harrison et al., 1994). We have adopted this ideal error of 0.010 AOD for the MFRSR and

508   CIMEL sun photometer in Fig. 9A. The error bars of the 2D-MAX-DOAS are those discussed in

509   section 3.3.1. In general, the errors are smaller at high SZA, as discussed in Sect. 3.3.1, and the largest

510   errors are ~0.012 at noon. The comparison of the AOD_{430} retrieved by DOAS compares well, and is

511   generally within the combined error bars with the other measurements. The comparison is best in the

512   morning, and DOAS agrees better with the MFRSR throughout the day; there is only marginal

513   agreement with the CIMEL sun photometer in the afternoon. At noon, there is a small increase in

514   AOD_{430} of about 0.05 and the response of this change is greater for the 2D-MAX-DOAS than for the

515   MFRSR and Sun photometer likely due to maximum sensitivity to small changes in AOD. A power

516   outage inside the seatainer restricted measurements after 17:30 LST.

517

518   The average diurnal difference of AOD_{430} (relative to the 2D-MAX-DOAS) on 22 July is +0.0199 ±

519   0.014 (CIMEL), +0.003 ± 0.019 (MFRSR), and -0.011 ± 0.014 during the overpass of the HSRL-2.

520   The AOD_{430} measured by HSRL-2 during two overpasses is slightly lower than the AOD_{430} measured

521   by the CIMEL sun photometer, agrees closely in one instance with the 2D-MAX-DOAS, and the

522   closest agreement is observed for MFRSR. Note that the HSRL AOD values correspond to the layer

523   between the surface and about 7 km. In general, 90 to 95 % of the aerosol extinction is estimated to be

Atmospheric
Measurement
Techniques
Discussions

524   below the ~ 7 km. The average diurnal difference in AOD_{430} shows that the CIMEL sun photometer is

525   0.017 greater than MFRSR. In general a good agreement is reflected in the linear correlation analysis

526   between the 2D-MAX-DOAS and CIMEL sun photometer: $DOAS_{AOD}$ = -(0.013 ± 0.010) + (0.96 ±

527   0.09)·$CIMEL_{AOD}$ (R^2 = 0.82); between 2D-MAX-DOAS and MFRSR: $DOAS_{AOD}$ = -(0.029 ± 0.020) +

528   (1.32 ± 0.21)·$MFRSR_{AOD}$ (R^2 = 0.64); and between CIMEL sun photometer and MFRSR: $CIMEL_{AOD}$

529   = -(0.028 ± 0.009) + (1.45 ± 0.10)·$MFRSR_{AOD}$ (R^2 = 0.91). Notably, the offset is larger than 0.02 in

530   some instances, highlighting the importance of instrument comparisons under low AOD conditions.

531

532   On 17 July the AOD_{430} reached values of 0.6 at noon (Fig. 9B). The high AOD and low RSP signal

533   from 11:00 to 14:00 LST limited the retrieval of AOD and g from the 2D-MAX-DOAS. As shown in

534   Fig. 7 the RSP decreases significantly at high AOD and low SZA likely due to dominance of multiple

535   aerosol forward scattering. On this day averaged RSP values obtained with the solar azimuth scans

536   from ~11:00 to 14:00 were similar to the RSP error limiting the analysis. This could be circumvented

537   in the future by conducting almucantar scans at a lower EA. Under conditions when a retrieval is

538   warranted, the comparison of the difference in AOD_{430} (relative to the 2D-MAX-DOAS) is -0.027 ±

539   0.03 (CIMEL), +0.005 ± 0.027 (MFRSR). The AOD from CIMEL sun photometer is 0.035 ± 0.015

540   greater than that from MFRSR. The linear correlation between the 2D-MAX-DOAS and CIMEL sun

541   photometer is: $DOAS_{AOD}$ = -(0.017 ± 0.034) + (0.95 ± 0.08) x $CIMEL_{AOD}$ (R^2 = 0.88); between 2D-

542   MAX-DOAS and MFRSR: $DOAS_{AOD}$ = -(0.025 ± 0.027) + (1.00 ± 0.07) x $MFRSR_{AOD}$ (R^2 = 0.91);

543   and between CIMEL sun photometer and MFRSR: $CIMEL_{AOD}$ = -(0.020 ± 0.015) + (1.03 ± 0.04) x

544    $MFRSR_{AOD}$ (R^2 = 0.97).

545

546   Clearly under high AOD conditions the maximum AOD diurnal difference of ~ 0.027 accounts for less

547   than 5 % of the AOD. On the other hand, the diurnal differences between instruments under low AOD

548   account (~0.02) for about 20 % of the AOD. Overall good agreement is reflected in the linear

549   regression analysis of pooled data from both case study days: $DOAS_{AOD}$ = -(0.019 ± 0.006) + (1.03 ±

550   0.02)·$CIMEL_{AOD}$ (R^2 = 0.98), $DOAS_{AOD}$ = -(0.006 ± 0.005) + (1.08 ± 0.02)·$MFRSR_{AOD}$ (R^2 = 0.98),

551   and $CIMEL_{AOD}$ = (0.013 ± 0.004) + (1.05 ± 0.01)·$MFRSR_{AOD}$ (R^2 = 0.99).

552

553   **3.7   Context with literature: advantages and limitations**

554   According to Holben et al. (1998) the AOD uncertainty of newly calibrated Sun photometers is ± 0.01

555   for typical visible wavelengths, and ± 0.02 for shorter wavelengths. In particular, the error in AOD

Atmospheric
Measurement
Techniques
Discussions

556 becomes highly sensitive to the calibration error at low AOD. For example, for $AOD_{440} < 0.05$ and 5%

557 calibration error the AOD uncertainty can reach 44 %. On the other hand, the error in AOD decreases

558 dramatically for the same calibration error if solar scattering measurements are used (Holben et al.

559 1998). Our innovative retrieval strategy for AOD and g is based on solar scattered light, but

560 circumvents the calibration uncertainty outlined above, and provides robust measurements under low

561 AOD conditions. Our measurements are inherently calibrated, i.e., do not require radiance calibration

562 which is subject to drift, and needs frequent sensor attention during field operation. The RSP-based

563 retrievals only rely on relative radiance measurements in the SRAA and hyperspectral domain, which

564 makes them particularly useful for long-term observations in remote environments.

565 The diurnal error in AOD of direct sun transmission measurements is also subject to the optical path

566 through the Earth's atmosphere. In general, the nominal error in AOD will change with the air mass

567 factor (cos(SZA)) and potentially needs to be scaled accordingly leaving smaller errors at high SZA

568 (Sinyuk et al., 2012). One important advantage of RSP-based retrievals is that the aerosol information

569 content is enhanced at low AOD. RSP constraints to column aerosol optical properties are

570 complementary to O_2-O_2 measurements that are widely used to infer information about clouds and

571 aerosols (Baidar et al., 2013; Gielen et al., 2014; Wagner et al., 2014; Ortega et al., 2015b; Volkamer et

572 al., 2015). The synergistic use of RSP and O_2-O_2 holds great potential to better assess profile and

573 column properties of aerosols and clouds, and currently remains largely unexplored.

574 **4.   Summary and conclusions**

575 In this work we present a detailed analysis of RRS using direct sun and solar almucantar

576 measurements of scattered solar photons by the CU 2D-MAX-DOAS instrument (see part 1, Ortega et

577 al., 2015a). The rapid solar azimuth scan, i.e., integration time of 1 s and total acquisition time of ~2

578 min to measure from -180˚ to 180˚ SRAA in steps of 5˚ relative to the sun, provide robust means to

579 simultaneously retrieve AOD and the column integrated aerosol phase function (simplified by the

580 asymmetry parameter, g). We conclude the following:

581 • Measurements of RSP have maximum sensitivity towards retrieving AOD and g under

582 molecular scattering conditions. This is demonstrated with RTM simulations of the RSP using

583 diurnal solar azimuth geometry. The highest sensitivity towards both g and AOD is achieved if

584 using small SRAA ($\leq 5˚$).

585 • The error in the RSP based retrieval of AOD and g is limited by the uncertainty about RSP

Atmospheric
Measurement
Techniques
Discussions

586   contained in the reference spectrum. We minimize the error by retrieving near-absolute RSP

587   using a direct sun reference spectrum recorded with the same instrument. The direct sun

588   spectrum is also affected by RRS. We estimate $RSP_{DS} = 0.44 \pm 0.22$ %, compared to $RSP_{zenith} =$

589   2.34 ± 0.22 % ($SZA = 28°$, $AOD_{430} = 0.11$). Direct sun observations at low SZA systematically

590   minimize RSP, and are most valuable for precise AOD and g retrievals.

591   •   RSP based retrievals of AOD and g have higher sensitivity at high SZAs, and low AOD. This is

592   complementary to existing techniques that operate on solar transmission. The absolute error are

593   about 0.02, 0.004, 0.0025 and 0.0005 for AOD_{430} of 0.4, 0.1, 0.05 and 0.01, respectively (4-

594   5 % relative error), at $SZA = 35°$. The errors decrease with increasing SZA, and absolute errors

595   are 0.014, 0.003, 0.002, and 0.0004 for AOD_{430} of 0.4, 0.1, 0.05 and 0.01, respectively (3-4 %

596   relative error), at $SZA = 70°$.

597   •   Retrievals based on RSP measurements at a subset of SRAA hold potential to measure AOD

598   under broken cloud conditions. Clear sky and broken cloud conditions can be identified using

599   the color index, and AOD retrievals under such conditions warrant further study.

600   •   The RSP retrieval of AOD and g consist is inherently calibrated, since it relies only on relative

601   intensity changes that are measured in the hyperspectral domain, and at various SRAA.

602   Combined with the high sensitivity at low AOD and high SZA makes measurements of RSP

603   particularly useful to conduct long-term time series measurements in remote environments,

604   such as the arctic, or remote ocean environments at tropical latitudes.

605   •   The retrieval strategies may be optimized by conducting azimuth scans with longer integration

606   time, at solar EA and lower EAs, and by conducting EA scans for a larger subset of SRAA to

607   simultaneously measure azimuth distributions and vertical profiles of trace gases. 2D-MAX-

608   DOAS measurements in the solar principal plane sky geometry (similar to the almucantar scan)

609   would further increase the sensitivity towards the lower part of the atmosphere.

Atmospheric
Measurement
Techniques
Open Access
Discussions
EGU

622

References

624
625   Augustine, J. A., Hodges, G. B., Dutton, E. G., Michalsky, J. J., and Cornwall, C. R.: An aerosol optical
626   depth climatology for NOAA's national surface radiation budget network (SURFRAD), Journal of
627   Geophysical Research: Atmospheres, 113, D11204, doi:10.1029/2007JD009504., 2008.
628
629   Baidar, S., H. Oetjen, S. Coburn, B. Dix, I. Ortega, R. Sinreich, and R. Volkamer. The CU Airborne
630   MAX-DOAS Instrument: Vertical Profiling of Aerosol Extinction and Trace Gases. , Atmospheric
631   Measurement Techniques, 6(3), 719-719-739, 2013. doi: 10.5194/amt-6-719-2013
632
633   Baidar, S., Kille, N., Ortega, I., Sinreich, R., Thomson, D., Hannigan, J., and Volkamer, R.:
634   Development of a digital mobile solar tracker, Atmos. Meas. Tech. Discuss., 8, 11401-11427,
635   doi:10.5194/amtd-8-11401-2015, 2015.
636
637   Berg, L., Fast, J., Barnard, J., Burton, S., Cairns, B., Chand, D., Comstock, J., Dunagan, S., Richard, F.,
638   Flynn, C., Hair, J., Hostetler, C., Hubbe, J., Jefferson, A., Johnson, R., Kassianov, E., Kluzek, C.,
639   Kollias, P., Lamer, K., Lantz, K., Mei, F., Miller, M., Michalsky, J., Ortega, I., Pekour, M., Rogers, R.,
640   Russell, P., Redemann, P., Sedlacek, A., Segal-Rosenheimer, M., Schmid, B., Shilling, J., Shinozuka,
641   Y., Springston, S., Tomlinson, J., Tyrrell, M., Wilson, J., Volkamer, R., and Zelenyuk, A.: The Two-
642   Column Aerosol Project: Phase I Overview and Impact of Elevated Aerosol Layers on Aerosol Optical
643   Depth, submitted to Journal of Geophysical Research: Atmospheres., 2015.
644
645   Bodhaine, B. A., Wood, N. B., Dutton, E. G., and Slusser, J. R.: On Rayleigh Optical Depth
646   Calculations, Journal of Atmospheric and Oceanic Technology, 16, 1854-1861, 1999.
647
648   Bogumil, K., Orphal, J., Homann, T., Voigt, S., Spietz, P., Fleischmann, O., Vogel, A., Hartmann, M.,
649   Kromminga, H., Bovensmann, H., Frerick, J., and Burrows, J.: Measurements of molecular absorption
650   spectra with the SCIAMACHY pre-flight model: instrument characterization and reference data for
651   atmospheric remote-sensing in the 2302380 nm region, Journal of Photochemistry and Photobiology A:
652   Chemistry, 157, 167 − 184, doi:10.1016/S1010-6030(03)00062-5, 2003.
653
654   Bohren, C. F. and Huffman, D. R.: Absorption and Scattering of Light by Small Particles, Wiley, 1998.
655
656   Box, M. A. and Deepak, A.: Retrieval of aerosol size distributions by inversion of simulated aureole
657   data in the presence of multiple scattering, Appl. Opt., 18, 1376–1382, 1979.
658
659   Chance, K. V. and Spurr, R. J. D.: Ring effect studies: Rayleigh scattering, including molecular
660   parameters for rotational Raman scattering, and the Fraunhofer spectrum, Appl. Opt., 36, 5224–5230,
661   doi: 10.1364/AO.36.005224, 1997.
662
663   Chung, C. E., Ramanathan, V., Kim, D., and Podgorny, I. A.: Global anthropogenic aerosol direct

Atmospheric
Measurement
Techniques
Open Access
Discussions
EGU

664   forcing derived from satellite and ground-based observations, Journal of Geophysical Research:
665   Atmospheres, 110, D24207, doi:10.1029/2005JD006356., 2005.
666
667   Clémer, K., Van Roozendael, M., Fayt, C., Hendrick, F., Hermans, C., Pinardi, G., Spurr, R., Wang, P.,
668   and De Mazière, M.: Multiple wavelength retrieval of tropospheric aerosol optical properties from
669   MAXDOAS measurements in Beijing, Atmos. Meas. Tech., 3, 863-878, doi:10.5194/amt-3-863-2010,
670   2010.
671
672   Deutschmann, T., Beirle, S., Frieß, U., Grzegorski, M., Kern, C., Kritten, L., Platt, U., Prados-Roman,
673   C., Puckimacrte, J.,Wagner, T.,Werner, B., and Pfeilsticker, K.: The Monte Carlo atmospheric radiative
674   transfer model McArtim: Introduction and validation of Jacobians and 3D features, J. Quant. Spectrosc.
675   Radiat. Transfer, 112, 1119–1137, doi:10.1016/j.jqsrt.2010.12.009, 2011.
676
677   Dubovik, O., Smirnov, A., Holben, B. N., King, M. D., Kaufman, Y. J., Eck, T. F., and Slutsker, I.:
678   Accuracy assessments of aerosol optical properties retrieved from Aerosol Robotic Network
679   (AERONET) Sun and sky radiance measurements, Journal of Geophysical Research: Atmospheres,
680   105(D8), 9791–9806, doi:10.1029/2000JD900040., 2000.
681
682   Eck, T. F., Holben, B. N., Reid, J. S., Dubovik, O., Smirnov, A., O'Neill, N. T., Slutsker, I., and Kinne,
683   S.: Wavelength dependence of the optical depth of biomass burning, urban, and desert dust aerosols,
684   Journal of Geophysical Research: Atmospheres, 104(D24), 31333–31349, doi:10.1029/1999JD900923.,
685   1999.
686
687   Fayt, C. and Van Roozendael, M.: WinDOAS 2.1, Software User Manual, Belgian Institute for Space
688   Aeronomy, Brussels, Belgium, available at: http://uv-vis.aeronomie.be/software/WinDOAS/WinDOAS-
689   SUM-210b.pdf (last access: 29 May 2012), 2001.
690
691   Frieß, U., Monks, P. S., Remedios, J. J., Rozanov, A., Sinreich, R., Wagner, T., and Platt, U.: MAX-
692   DOAS O_4 measurements: A new technique to derive information on atmospheric aerosols: 2. Modeling
693   studies, Journal of Geophysical Research (Atmospheres), 111, D14 203, doi:10.1029/2005JD006618,
694   2006.
695
696   Gielen, C., Van Roozendael, M., Hendrick, F., Pinardi, G., Vlemmix, T., De Bock, V., De Backer, H.,
697   Fayt, C., Hermans, C., Gillotay, D., and Wang, P.: A simple and versatile cloud-screening method for
698   MAX-DOAS retrievals, Atmos. Meas. Tech., 7, 3509-3527, doi:10.5194/amt-7-3509-2014, 2014.
699
700   Gisi, M., Hase, F., Dohe, S., and Blumenstock, T.: Camtracker: a new camera controlled high precision
701   solar tracker system for FTIR-spectrometers, Atmos. Meas. Tech., 4, 47-54, doi:10.5194/amt-4-47-
702   2011, 2011.
703
704   Grainger, J. and Ring, J.: Anomalous Fraunhofer Line Profiles, Nature, 193, 762,
705   doi:10.1038/193762a010.1038/193762a0, 1962.
706
707   Hair, J. W., C. A. Hostetler, A. L. Cook, D. B. Harper, R. A. Ferrare, T. L. Mack, W. Welch, L. R.
708   Izquierdo, and F. E. Hovis.: Airborne High Spectral Resolution Lidar for profiling aerosol optical
709   properties, Appl. Opt., 47(36), 6734-6752, 2008.
710
711   Hansen, J., Sato, M., Nazarenko, L., Ruedy, R., Lacis, A., Koch, D., Tegen, I., Hall, T., Shindell, D.,

Atmospheric
Measurement
Techniques
Open Access
Discussions
EGU

712 Santer, B., Stone, P., Novakov, T., Thomason, L., Wang, R., Wang, Y., Jacob, D., Hollandsworth, S.,
713 Bishop, L., Logan, J., Thompson, A., Stolarski, R., Lean, J., Willson, R., Levitus, S., Antonov, J.,
714 Rayner, N., Parker, D., and Christy, J.: Climate forcings in Goddard Institute for Space Studies SI2000
715 simulations, Journal of Geophysical Research: Atmospheres, 107(D18), 4347,
716 doi:10.1029/2001JD001143, 2002.
717
718 Harrison, L., Michalsky, J., and Berndt, J.: Automated multi-filter rotation shadow-band radiation
719 measurements, Appl. Opt., 33, 5118, 1994.
720
721 Herman, J., A. Cede, E. Spinei, G. Mount, M. Tzortziou, and N. Abuhassan.: NO_2 column amounts
722 from ground-based Pandora and MFDOAS spectrometers using the direct sun DOAS technique:
723 Intercomparisons and application to OMI validation, J. Geophys. Res., 114, D13307,
724 doi:10.1029/2009JD011848, 2009.
725
726 Holben, B., Eck, T., Slutsker, I., Tanré, D., Buis, J., Setzer, A., Vermote, E., Reagan, J., Kaufman,
727 Y., Nakajima, T., Lavenu, F., Jankowiak, I., and Smirnov, A.: AERONET—A Federated Instrument
728 Network and Data Archive for Aerosol Characterization, Remote Sensing of Environment, 66, 1 – 16,
729 doi:10.1016/S0034-4257(98)00031-5, 1998.
730
731 Holben, B. N., Tanr´e, D., Smirnov, A., Eck, T. F., Slutsker, I., Abuhassan, N., Newcomb, W. W.,
732 Schafer, J. S., Chatenet, B., Lavenu, F., Kaufman, Y. J., Castle, J. V., Setzer, A., Markham, B., Clark,
733 D., Frouin, R., Halthore, R., Karneli, A., O'Neill, N. T., Pietras, C., Pinker, R. T., Voss, K., and Zibordi,
734 G.: An emerging ground-based aerosol climatology: Aerosol optical depth fromAERONET, Journal of
735 Geophysical Research: Atmospheres, 106, 12 067–12 097, doi: 10.1029/2001JD900014, 2001.
736
737 Hönninger, G., von Friedeburg, C., and Platt, U.: Multi axis differential optical absorption spectroscopy
738 (MAX-DOAS), Atmos. Chem. Phys., 4, 231-254, doi:10.5194/acp-4-231-2004, 2004.
739
740 Intergovernmental Panel on Climate Change: Climate Change 2013: The Physical Science Basis,
741 Cambridge University Press, Cambridge, United Kingdom and New York, NY, USA, 2013.
742
743 Kassianov, E., Barnard, J., Flynn, C., Riihimaki, L., Michalsky, J., and Hodges, G.: Areal-Averaged
744 Spectral Surface Albedo from Ground-Based Transmission Data Alone: Toward an Operational
745 Retrieval, Atmosphere, 5, 597, doi:10.3390/atmos5030597, 2014.
746
747 Kaufman, Y. J., A. Gitelson, A. Karnieli, E. Ganor, R. S. Fraser, T. Nakajima, S. Mattoo, and B. N.
748 Holben, Size distribution and scattering phase function of aerosol particles retrieved from sky
749 brightness measurements, J. Geophys. Res., 99(D5), 10341–10356, doi:10.1029/94JD00229, 1994.
750
751 Mao, K., Ma, Y., Xia, L., Chen, W. Y., Shen, X., He, T., and Xu, T.: Global aerosol change in the last
752 decade: An analysis based on MODIS data, Atmospheric Environment, 94, 680 – 686,
753 doi:10.1016/j.atmosenv.2014.04.053, 2014.
754
755 McComiskey, A., Schwartz, S. E., Schmid, B., Guan, H., Lewis, E. R., Ricchiazzi, P., and Ogren, J. A.:
756 Direct aerosol forcing: Calculation from observables and sensitivities to inputs, Journal of Geophysical
757 Research: Atmospheres, 113, doi:10.1029/2007JD009170, 2008.
758
759 Michalsky, J., Denn, F., Flynn, C., Hodges, G., Kiedron, P., Koontz, A., Schlemmer, J., and Schwartz,
760 S. E.: Climatology of aerosol optical depth in north-central Oklahoma: 1992–2008, Journal of

Atmospheric
Measurement
Techniques

Open Access

Discussions

761   Geophysical Research: Atmospheres, 115, doi:10.1029/2009JD012197, 2010.
762
763   Müller, D., Hostetler, C. A., Ferrare, R. A., Burton, S. P., Chemyakin, E., Kolgotin, A., Hair, J. W.,
764   Cook, A. L., Harper, D. B., Rogers, R. R., Hare, R. W., Cleckner, C. S., Obland, M. D., Tomlinson, J.,
765   Berg, L. K., and Schmid, B.: Airborne Multiwavelength High Spectral Resolution Lidar (HSRL-2)
766   observations during TCAP 2012: vertical profiles of optical and microphysical properties of a
767   smoke/urban haze plume over the northeastern coast of the US, Atmospheric Measurement Techniques,
768   7, 3487–3496, doi:10.5194/amt-7-3487-2014, 2014.
769
770   Nakajima, T., Tanaka, M., and Yamauchi, T.: Retrieval of the optical properties of aerosols from aureole
771   and extinction data, Appl. Opt., 22, 2951–2959, 1983.
772
773   Nakajima, T., Tonna, G., Rao, R., Boi, P., Kaufman, Y., and Holben, B.: Use of sky brightness
774   measurements from ground for remote sensing of particulate polydispersions, Appl. Opt., 35, 2672,
775   doi:10.1364/AO.35.002672, 1996.
776
777   Ortega, I., Koenig, T., Sinreich, R., Thomson, D., and Volkamer, R.: The CU 2-D-MAX-DOAS
778   instrument – Part 1: Retrieval of 3-D distributions of NO_2 and azimuth-dependent OVOC ratios,
779   Atmos. Meas. Tech., 8, 2371-2395, doi:10.5194/amt-8-2371-2015, 2015a.
780
781   Ortega, I., Berg, L., Ferrare, R., Johnathan, H., Hostetler, C., and Volkamer, R.: The effect of elevated
782   aerosol layers on the apparent O_2-O_2 absorption by ground based MAX-DOAS, submitted to J. Quant.
783   Spectr. Radiat. Transf., 2015b.
784
785   Platt, U. and Stutz, J.: Differential Optical Absorption Spectroscopy, 597 pp., Springer, Berlin,
786   doi:10.1007/978-3-540-75776-4, 2008.
787
788   Remer, L. A., Kleidman, R. G., Levy, R. C., Kaufman, Y. J., Tanré, D., Mattoo, S., Martins, J. V.,
789   Ichoku, C., Koren, I., Yu, H., and Holben, B. N.: Global aerosol climatology from the MODIS satellite
790   sensors, Journal of Geophysical Research: Atmospheres, 113, doi: 10.1029/2007JD009661, 2008.
791
792   Sinreich, R., Coburn, S., Dix, B., and Volkamer, R.: Ship-based detection of glyoxal over the remote
793   tropical Pacific Ocean, Atmos. Chem. Phys., 10, 11359-11371, doi:10.5194/acp-10-11359-2010, 2010.
794
795   Sinyuk, A., Holben, B. N., Smirnov, A., Eck, T. F., Slutsker, I., Schafer, J. S., Giles, D. M., and
796   Sorokin, M.: Assessment of error in aerosol optical depth measured by AERONET due to aerosol
797   forward scattering, Geophysical Research Letters, 39, doi: 10.1029/2012GL05389410, 2012.
798
799   Torres, B., Toledano, C., Berjo´n, A., Fuertes, D.,Molina, V., Gonzalez, R., Canini,M., Cachorro, V. E.,
800   Goloub, P., Podvin, T., Blarel, L., Dubovik, O., Bennouna, Y., and de Frutos, A. M.: Measurements on
801   pointing error and field of view of Cimel-318 Sun photometers in the scope of AERONET,
802   Atmospheric Measurement Techniques, 6, 2207–2220, 2013.
803
804   Vogel, L., Sihler, H., Lampel, J., Wagner, T., and Platt, U.: Retrieval interval mapping: a tool to
805   visualize the impact of the spectral retrieval range on differential optical absorption spectroscopy
806   evaluations, Atmospheric Measurement Techniques, 6, 275–299, doi:10.5194/amt-6-275-2013, 2013.
807
808   Volkamer, R., Baidar, S., Campos, T. L., Coburn, S., DiGangi, J. P., Dix, B., Eloranta, E. W., Koenig, T.
809   K., Morley, B., Ortega, I., Pierce, B. R., Reeves, M., Sinreich, R., Wang, S., Zondlo, M. A., and

Atmospheric
Measurement
Techniques
Discussions

Open Access

810   Romashkin, P. A.: Aircraft measurements of BrO, IO, glyoxal, NO_2, H_2O, O_2–O_2 and aerosol extinction
811   profiles in the tropics: comparison with aircraft-/ship-based in situ and lidar measurements, Atmos.
812   Meas. Tech., 8, 2121-2148, doi:10.5194/amt-8-2121-2015, 2015.

814   Wagner, T., Dix, B., Friedeburg, C. v., Frieß, U., Sanghavi, S., Sinreich, R., and Platt, U.: MAX-DOAS
815   O_4 measurements: A new technique to derive information on atmospheric aerosols-Principles and
816   information content, Journal of Geophysical Research (Atmospheres), 109, D22 205,
817   doi:10.1029/2004JD004904, 2004.

819   Wagner, T., Burrows, J. P., Deutschmann, T., Dix, B., von Friedeburg, C., Frieß, U., Hendrick, F.,
820   Heue, K., Irie, H., Iwabuchi, H., Kanaya, Y., Keller, J., McLinden, C. A., Oetjen, H., Palazzi, E.,
821   Petritoli, A., Platt, U., Postylyakov, O., Pukite, J., Richter, A., van Roozendael, M., Rozanov, A.,
822   Rozanov, V., Sinreich, R., Sanghavi, S., andWittrock, F.: Comparison of box-air-mass-factors and
823   radiances for Multiple-Axis Differential Optical Absorption Spectroscopy (MAX-DOAS) geometries
824   calculated from different UV/visible radiative transfer models, Atmospheric Chemistry and Physics, 7,
825   1809–1833, 2007.

827   Wagner, T., Beirle, S., and Deutschmann, T.: Three-dimensional simulation of the Ring effect in
828   observations of scattered sun light using Monte Carlo radiative transfer models, Atmos. Meas. Tech., 2,
829   113–124, doi:10.5194/amt-2-113-2009, 2009a.

831   Wagner, T., Deutschmann, T., and Platt, U.: Determination of aerosol properties from MAX-DOAS
832   observations of the Ring effect, Atmos. Meas. Tech., 2, 495-512, doi:10.5194/amt-2-495-2009, 2009b.

834   Wagner, T., Beirle, S., Deutschmann, T., and Penning de Vries, M.: A sensitivity analysis of Ring effect
835   to aerosol properties and comparison to satellite observations, Atmos. Meas. Tech., 3, 1723-1751,
836   doi:10.5194/amt-3-1723-2010, 2010.

838   Wagner, T., Apituley, A., Beirle, S., Dörner, S., Friess, U., Remmers, J., and Shaiganfar, R.: Cloud
839   detection and classification based on MAX-DOAS observations, Atmos. Meas. Tech., 7, 1289-1320,
840   doi:10.5194/amt-7-1289-2014, 2014.

842   Wang, Y., Li, A., Xie, P. H., Wagner, T., Chen, H., Liu, W. Q., and Liu, J. G.: A rapid method to derive
843   horizontal distributions of trace gases and aerosols near the surface using multi-axis differential optical
844   absorption spectroscopy, Atmos. Meas. Tech., 7, 1663-1680, doi:10.5194/amt-7-1663-2014, 2014.

846   Westervelt, D. M., Horowitz, L. W., Naik, V., and Mauzerall, D. L.: Radiative forcing and climate
847   response to projected 21st century aerosol decreases, Atmos. Chem. Phys. Discuss., 15, 9293-9353,
848   doi:10.5194/acpd-15-9293-2015, 2015.

849   **Tables:**

850

851   Table 1. Suite of measurements and products used in this work.

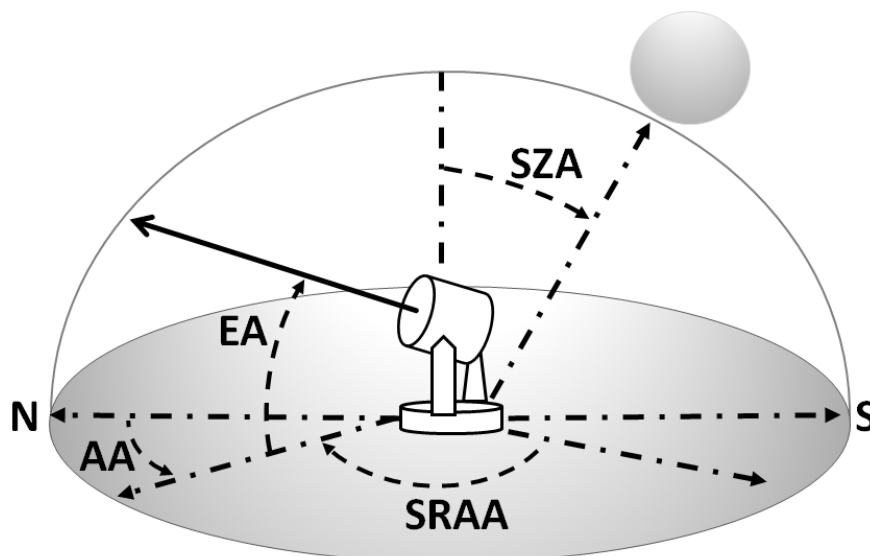| Ground based instruments				
Instrument	**Principle of measurement**	**Absolute radiometric calibration (YES/NO)**	**Products**	**Reference**
2D-MAX-DOAS	Solar scattered light	NO	AOD and g (430 nm)	Ortega et al. (2015a)
MFRSR	Total and diffuse solar irradiances	YES	AOD (430 nm) calculated using the Angstrom exponent between the standard wavelengths of 415 and 500 nm.	Harrison et al. (1994)
CIMEL sun photometer	Direct solar beam and diffused sky radiation	YES	Level 2.0: AOD (430 nm) calculated using the Angstrom exponent between the standard wavelengths of 340 and 440 nm and g (440 nm)	Holben et al. (1998)
Radiosondes	Weather balloon that measures various atmospheric parameters	N/A	Vertical profiles of temperature, pressure and humidity (4 times/day)	Berg et al. (2015)
Airborne instruments				
HSRL-2	backscatter and extinction coefficients		AOD (430 nm) - calculated using the Angstrom exponent between the standard wavelengths of 355 and 532 nm.	Muller et al. (2014)

852

853   Table 2. Geometry of measurements and configuration used during the TCAP field campaign.

Mode	EA (°)	AA (°)	SRAA (°)	Total acquisition Time (min)
1	1,3,6,8,10,30,45,90	0, 180	variable	16 - 17[a]
2	Solar elevation (90 – θ_0) and 45	variable	5, 10, 15. . . 180 (left and right)	2 - 3[b]
3	Solar elevation	variable	0	2 – 6

854   [a]Integration time of 60s at each α. [b]Integration time of 1s at each SRAA.

Atmospheric
Measurement
Techniques
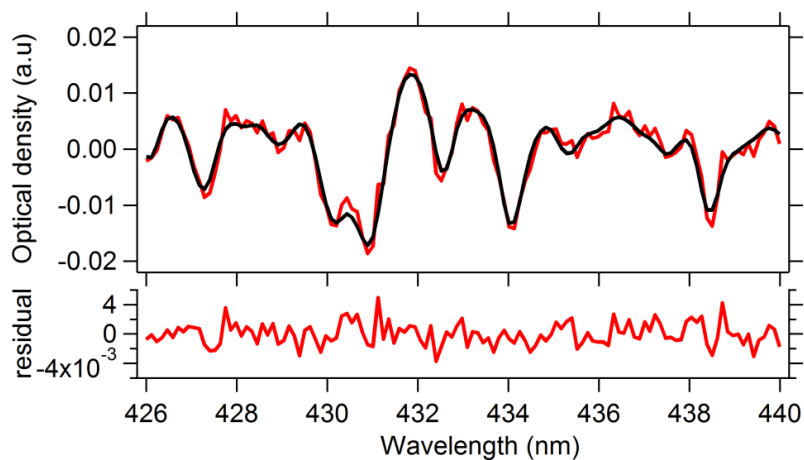
Open Access

EGU

Discussions
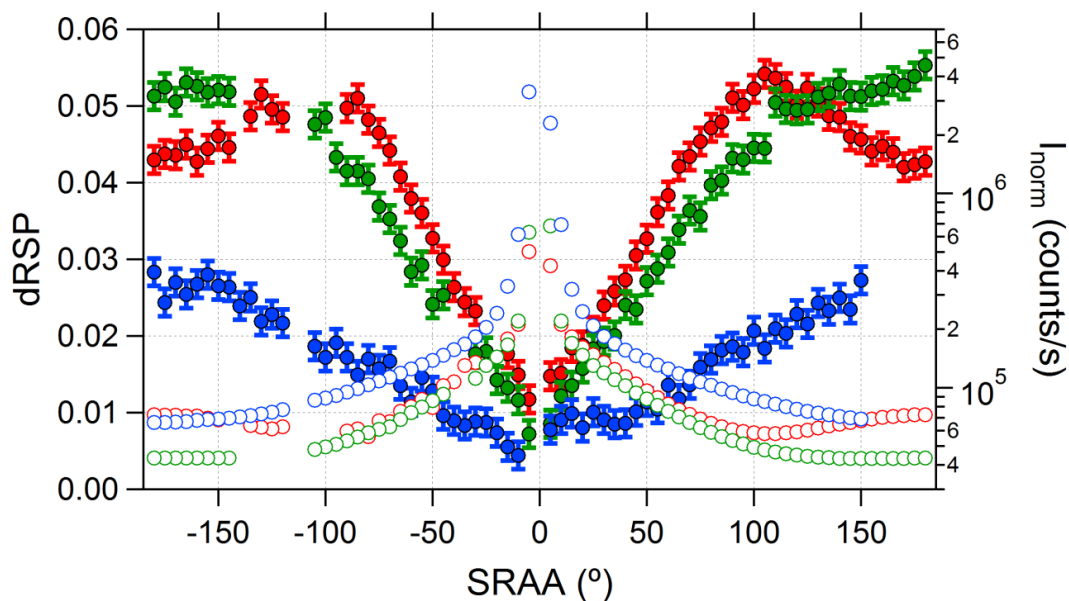
855   **Figures:**

856

857   Fig. 1. Sketch of measurement geometry used with the 2D-MAX-DOAS. The solid line coming out
858   from the telescope represents the azimuth angle (AA) with respect to North characterized by the
859   elevation angle (EA) and solar relative azimuth angle (SRAA). SZA is the solar zenith angle.
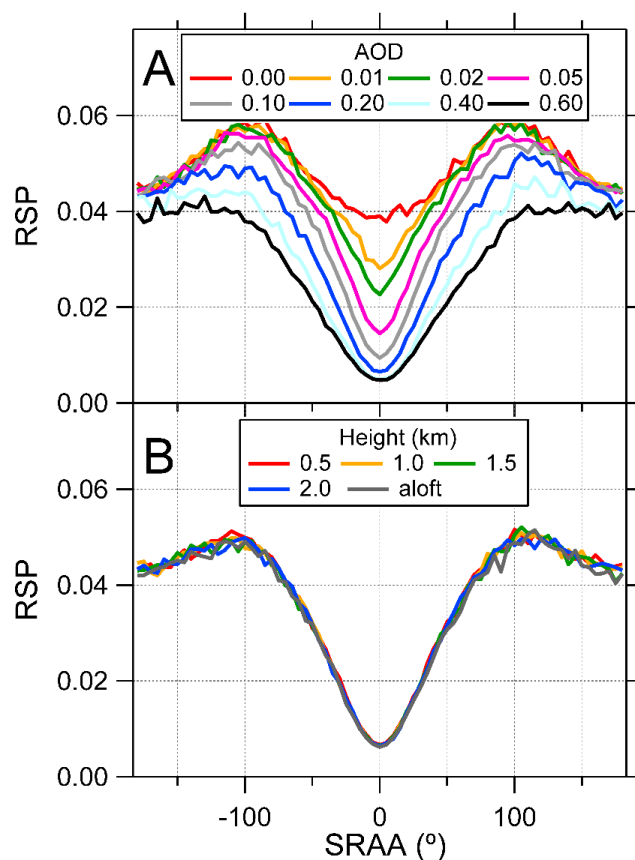

860

861   Fig. 2. Top: example of spectral proof for the detection of dRSP (1 s integration time) using the solar
862   azimuth scan on 22 July 2012 at 7:43 LST (SZA = 66.3˚, SRAA = 120˚, EA = solar EA). The red line
863   represents the measured spectra and black line is the fitted normalized Ring cross section. The dRSP is
864   0.0502 ± 0.0011. Bottom: residual from the DOAS fit, $RMS_{meas} = 1.58 \times 10^{-3}$, is in good agreement with
865   the shot-noise $RMS_{theo} = 1.40 \times 10^{-3}$ based on photon counting statistics.

Atmospheric
Measurement
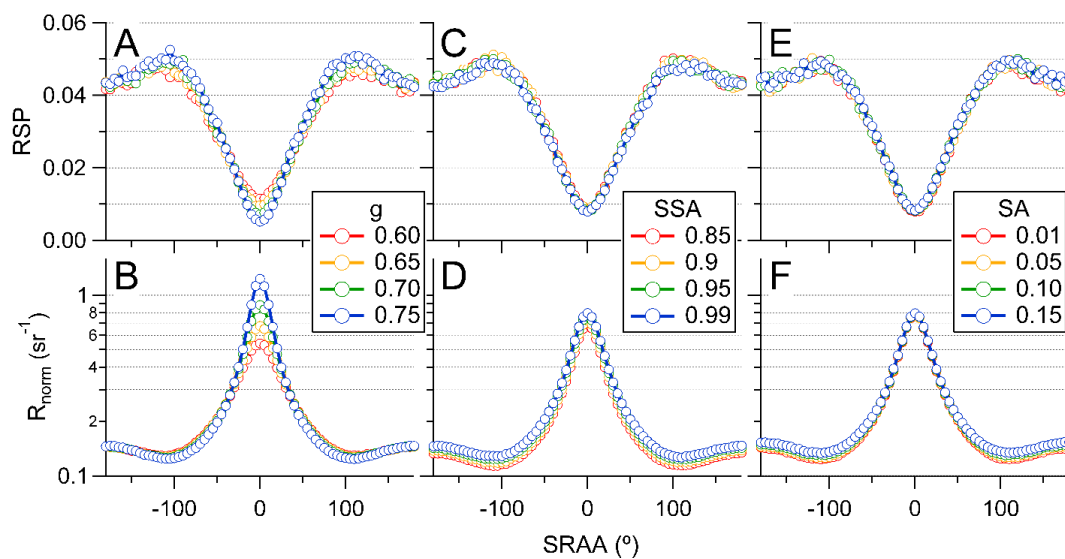Techniques
Discussions
Open Access

866
867   Fig 3. Example of the SRAA dependence of dRSP (filled circles) and I_{norm} (open circles) measured at

868   the solar elevation near 430 nm for three SZAs: (red) 66.5˚ (7:42 LST), (green) 49.0˚ (9:17 LST), and
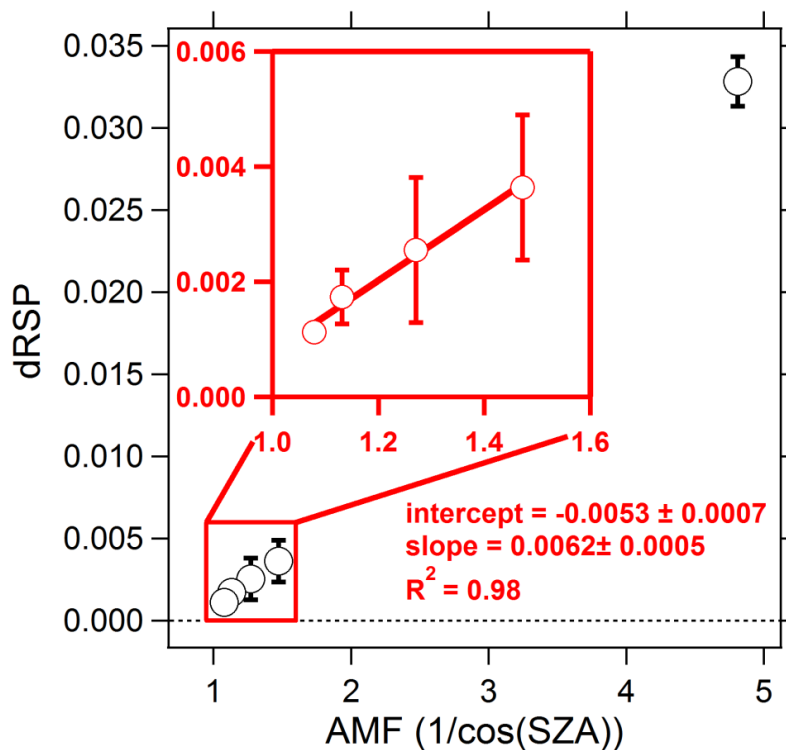
869   (blue) 22.0˚ (12:40 LST).

870

871

Fig. 4. Sensitivity study showing that simulated RSP (430 nm) is (A) a strong function of AOD, and (B)
insensitive to the aerosol vertical distribution. (A) AOD is varied, keeping aerosols homogeneously
distributed (box profile) up to 1.5 km altitude. (B) The aerosol extinction vertical distribution is varied
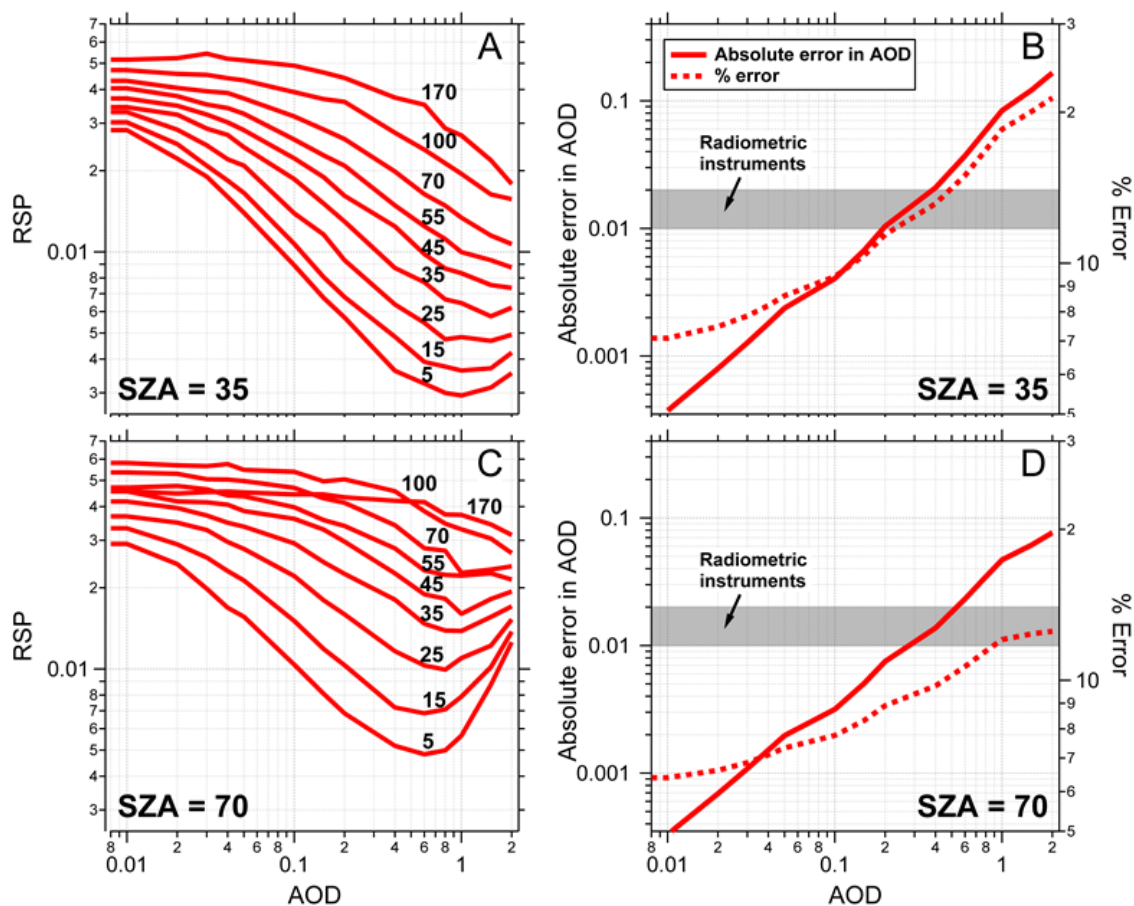for a constant AOD of 0.2. The simulation is for SZA = 70˚, SSA = 0.98, g = 0.70, SA = 0.05.

Atmospheric
Measurement
Techniques
Open Access
Discussions

876
877 Fig. 5. Sensitivity study showing simulated RSP (top row) and sun-normalized radiances, R_{norm} (sr^{-1})

878 defined as the ratio of the radiance ($W \cdot m^2 \cdot sr^{-1}$) in the geometry indicated to the solar irradiance ($W \cdot m^2$)

879 (bottom row) at 430 nm for several input parameters: (A, B) g, (C, D) SSA, and (E, F) SA. The

880 simulations were carried out assuming a box extinction profile (1.5 km height) with an AOD of 0.2, and

881 SZA = 70˚.

Atmospheric
Measurement
Techniques

Open Access

Discussions

EGU
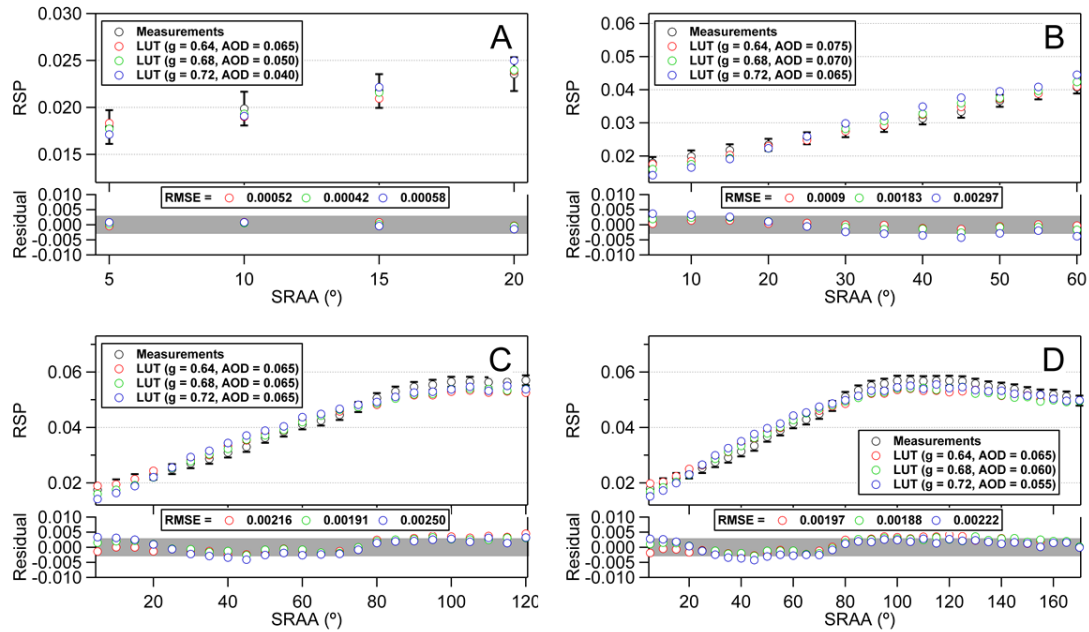

882

Fig. 6. Direct sun dRSP as a function of the air mass factor, AMF = 1/cos(SZA). All direct sun spectra

measured on 22 July 2012 were evaluated (SZA binned) relative to a direct sun reference spectrum

measured at SZA = 28°. The insert shows the zoom-in of the linear correlation plot used to

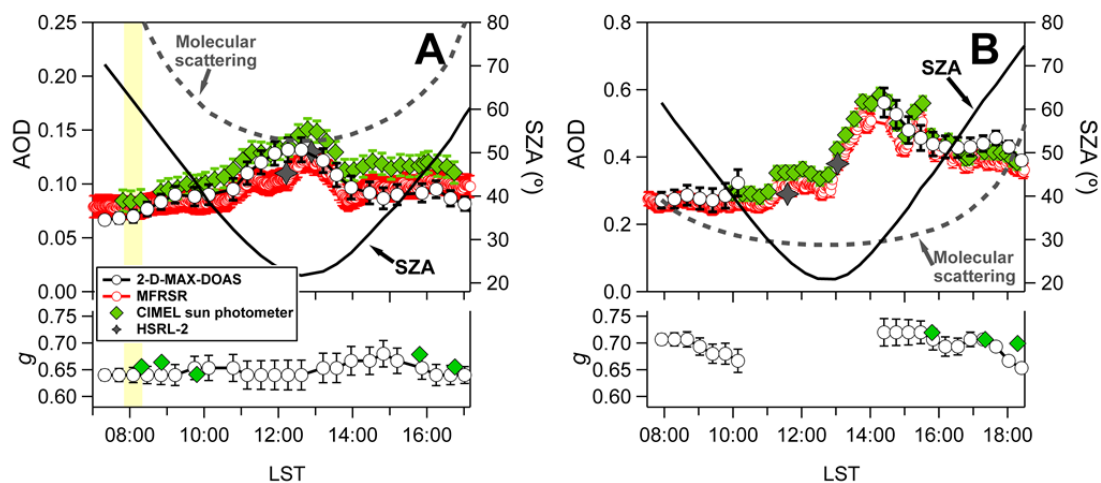quantitatively determine the offset at AMF = 0 (see text for details).

887

888   Fig 7. Simulated RSP as a function of AOD for 5˚ < SRAA < 100˚ at (A) SZA = 35˚, and (C) SZA =

889   70˚. Additional parameters are g = 0.72, SA = 0.05, SSA= 0.98. (B and D) Absolute error in AOD and

890   percentage error calculated with equation 3 (see text for details). An AOD error range of 0.01 − 0.02 is

891   indicated with the gray shadow area. A value of 0.01 is typical of newly radiometrically calibrated

892   instruments.

Atmospheric
Measurement
Techniques

Open Access

Discussions

EGU

893

894   Fig 8. Comparison of measured RSP (black open circles) and simulated RSP (open circles) with the

895   LUT using three different g (red: $g = 0.64$, green: $g = 0.68$, and blue: $g = 0.72$). The examples shown

896   here represent the best fit that minimizes equation 1 for different ranges of SRAA: (A) 5 to 20˚, (B) 5

897   to 60˚, (C) 5 to 120˚, and (D) 5 to 170˚ SRAA. The retrieved AOD in each case is indicated in the

898   labels.

899

Atmospheric
Measurement
Techniques
Open Access
Discussions
EGU

900

Fig 9. Time series of AOD comparing the 2D-MAX-DOAS with MFRSR, CIMEL sun photometer and

HSRL-2 under (A) low AOD case on 22 July and (B) under high AOD on 17 July. The dashed gray line

represents the molecular optical depth. The retrieved *g* from 2D-MAX-DOAS (430nm) and CIMEL

(440 nm) are shown in the bottom plot. The yellow shading in A represents the time period used in the

example of Fig. 8.